PHYSICAL REVIEW B **81**, 205302 (2010)

Direct photogeneration of biexcitons via virtual single-exciton and biexciton states in PbSe quantum dots

Leonardo Silvestri
Dipartimento di Scienza dei Materiali, Università degli Studi di Milano Bicocca, via Cozzi 53, I-20125 Milano, Italy

Vladimir M. Agranovich
Chemistry Department, University of Texas–Dallas, Dallas, Texas 75083, USA and Institute of Spectroscopy, Russian Academy of Science, Troitsk, Moscow Reg. 142190, Russia

(Received 2 November 2009; revised manuscript received 27 March 2010; published 4 May 2010)

Following the experimental observation that in semiconductor nanocrystals a single high-energy photon can generate multiple electron-hole pairs, several mechanisms have been proposed to explain such process of carrier multiplication (CM). Among them, impact ionization is currently considered as the most prominent mechanism in bulk semiconductors as well as in quantum dots (QDs). However, impact ionization is a multistep process which produces a delayed appearance of multiple excitons, and it cannot explain the instantaneous CM observed in PbSe QDs. In this work we present numerical simulations of the instantaneous mechanism of direct biexciton photogeneration via virtual exciton and biexciton states in PbSe QDs, which takes place only during the pump pulse excitation. The theoretical model is based on a four-band envelope-function calculation of electron and hole states in spherical PbSe QDs and treats Coulomb interaction in the framework of perturbation theory up to the first order. CM efficiency has been numerically evaluated for three different QD samples of various sizes and band structures, considering photon energies up to four times the QD energy gap. The results suggest that the mechanism of direct photogeneration can be only partially responsible for the total experimentally observed CM, which is the sum of instantaneous and delayed contributions. We show that the efficiency of such process strongly depends on the incident photon frequency, being particularly large in spectral regions of weak excitonic absorption. Our simulations also indicate that the virtual exciton channel is much more effective than the virtual biexciton channel and that the presence of a mirror symmetry between valence and conduction bands has only minor impact on the CM efficiency. Even if the contributions of instantaneous and impact generation still have not been experimentally separated, our numerical results are compared with available experimental data, and a detailed discussion of their dependence on the model parameters is presented.

DOI: 10.1103/PhysRevB.81.205302 PACS number(s): 78.67.Hc, 78.67.Bf, 73.21.La, 73.22.Dj

I. INTRODUCTION

In recent years, particularly after the publication of Schaller *et al.*[1,2] and Ellingson *et al.*[3] papers, the process of so-called carrier multiplication (CM) in PbSe and PbS quantum dots (QDs) has attracted great attention from the scientific community. This process, also known as multiple exciton generation (MEG), consists in the generation of more than one electron-hole (e-h) pair following the absorption of a single photon. In the above-cited papers, CM was detected by the transient absorption pump-probe method, and experimental results suggested that the phenomenon is general to nanocrystalline materials, as opposed to bulk materials where the CM efficiency was found to be weak.[4] Following these encouraging results, a wide range of materials has been investigated and efficient CM has also been reported in CdSe,[5,6] InAs,[7,8] and Si (Ref. 9) QDs. However, in deep contrast to previous reports, transient photoluminescence measurements by Nair *et al.*[10,11] demonstrated a very poor CM. The authors reported a maximum efficiency of about 1.25 e-h pairs generated per photon in PbSe and PbS nanocrystals[10] and even no evidence of CM in CdSe and CdTe nanocrystals.[11] This observation is supported by recent experimental results by Pijpers *et al.*[12] showing that, contrary to common expectations, for a given photon energy CM occurs more efficiently in bulk PbS and PbSe than in QDs of the same materials. Moreover, the carrier multiplication efficiencies measured for the bulk have been quantitatively reproduced by means of tight-binding calculations, which indicate that the reduced CM efficiency in quantum dots can be ascribed to the reduced density of states in these structures. We expect that all these observations will stimulate further experimental studies of CM in QDs.

Together with current experimental efforts, theoretical attempts to understand the nature of CM in QDs and to estimate its efficiency have also been performed. So far, several models have been proposed to describe CM in QDs (a review of these models can be found in Ref. 13), and we believe that all the proposed mechanisms contribute to the CM efficiency to a certain extent. The main task of the theory is therefore to estimate the role played by each mechanism in determining CM efficiency in QDs. This kind of knowledge will be also useful to predict the efficiency of CM in other nanostructures in case such problem becomes topical.

The first mechanism proposed to explain CM in QDs was impact ionization (Schaller and Klimov,[1] see also Refs. 14 and 15). According to this model CM takes place through two events: the first one is the absorption of a high-energy photon by the QD and the second one is the decay of the high-energy QD excited state to a state with few e-h pairs. In the impact ionization picture the appearance of new e-h pairs is therefore a multistep process, the simplest one being the two-step process of biexciton generation, and the lifetime of the high-energy QD excited state determines the delay in the appearance of multiple excitons. However, the analysis of the exciton population dynamics[2] indicates that CM is a process which is very close to an instantaneous appearance of multiple e-h pairs. That is why two other models have been proposed where the multiexciton states are directly photogenerated.

One direct CM mechanism, introduced by Ellingson *et al.*[3] and Shabaev *et al.*,[16] assumes that the strong electron-electron (e-e) interaction inside the QD breaks the single electron approximation for carriers with kinetic energy above the effective energy gap and determines the structure of high-energy excitations. According to this model, therefore, a single high-energy photon creates a coherent superposition of single and multiple exciton states of the same energy and the condition of dominant two-exciton generation by a single photon is that the thermalization rate of a single exciton is lower than both the biexciton thermalization rate and the exciton-biexciton e-e coupling. In the formulation of such idea the authors also assumed that "in quantum dots the rate of electron relaxation through electron-phonon interactions can be significantly reduced because of the discrete character of the electron-hole spectra [bottleneck effect], and the rate of Auger processes, including the inverse Auger process of exciton multiplication, is greatly enhanced owing to carrier confinement and the concomitantly increased electron-hole Coulomb interaction" (from Ref. 17, page 178). In a more recent paper (Allan and Delerue[13]) the authors also considered the extreme case where all multiexciton states created by a single photon of energy $\hbar\omega$ are so efficiently coupled by Coulomb interactions that the system has enough time to relax to the multiexcitons with the highest density of states at that energy. Such statistical approach is, in its spirit, similar to the one used by Fermi[18] to describe high-energy collisions of protons with production of multiple mesons. In the case of CM in quantum dots such approach postulates that the redistribution among excited states with energy $\hbar\omega$ is much faster than the phonon relaxation to lower-energy states. However, a recent study performed by Kilina *et al.*[19] demonstrates the breaking of the phonon bottleneck in PbSe and CdSe QDs, and fast relaxation to lower-energy states. The authors of this study stressed that not only recent experiments showed no bottleneck[20–23] but, in addition, their "time-domain *ab initio* study of the electron-phonon dynamics rationalizes the fast [energy] relaxation in PbSe and CdSe QDs, which have substantially different electronic properties. Atom fluctuations and surface effects lift degeneracies and create dense distributions of electronic levels at all but the lowest energies, while confinement enhances the electron-phonon coupling." They also explain that at higher energies the spacing between the electronic levels is of the order of the phonon frequencies, thus allowing the resonant energy exchange. These remarks, together with the experiments by Nair and Bawendi,[11] cast doubts on the correctness of the strong e-e interaction assumption in the investigated QDs.

Another mechanism which can also give direct photogeneration of multiple excitons in QDs was first mentioned in Ref. 2, and it assumes that a single high-energy photon creates final multiexciton states via virtual excitons, biexcitons, and other QD excited states. In this model, electron-electron interaction is treated in the framework of perturbation theory and, in order to estimate the rate of biexciton generation, all the possible virtual one-exciton[2] and biexciton[24] states have to be taken into account. When considering the generation of excited states with more than two e-h pairs, the number of virtual excited states sharply increases, making the calculation of the transition rates much more cumbersome.

In the present paper we develop this latter model[2] and present numerical calculations of biexciton generation rates and CM efficiencies in spherical PbSe QDs of different sizes. Due to computational limitations, we only consider the creation of excitons and biexcitons in the region between two and four times the QD energy gap (E_g), taking into account all the possible virtual excitonic and biexcitonic QD states.

We stress that direct, i.e., one step, photogeneration of final multiexciton states is an instantaneous process which takes place only during the pump pulse excitation. In transient absorption experiments pump pulse durations, τ_p, can be less than 100 fs. This is a short time compared with the impact ionization lifetimes, τ_i, calculated for PbSe QDs which, in the energy range we consider, are of the order of picoseconds.[15] In a sense, we can also say that our analysis concerns the precursor of the impact ionization process, in which some high-energy excited states are instantaneously generated by the pump pulse. Our numerical results show that biexcitons can be efficiently created at short times through the mechanism of direct photogeneration via virtual states. The predicted biexciton cross section at short times $t \approx \tau_p \ll \tau_i$ cannot explain the final efficiency at longer times, but it can be non-negligible at some excitation energies. Our approach, namely, an excitation via virtual states, can also be used in the impact ionization model, where it is important to know the initial distribution of high-energy excited states.

We found that the most important factors governing the instantaneous CM efficiency are the value of the e-e interaction matrix elements and the shape of the excitonic absorption spectra. In particular, we show that (a) only a small fraction of all the allowed biexcitonic states can be efficiently generated, (b) instantaneous CM efficiency is high only in regions where excitonic absorption is small, and (c) virtual excitons play a much more important role than virtual biexcitons.

In the following discussions we will always refer to the instantaneous CM and not to the CM efficiency at long times unless explicitly stated.

The paper is organized as follows. In Sec. II we find the eigenstates of PbSe spherical QDs in the single-particle approximation. In Sec. III we describe the model used to compute the CM efficiency. Numerical results are presented and discussed in Sec. IV, while Sec. V is devoted to conclusions. Finally, in the Appendix, we report the details of the calculations of transition dipole moments and e-e interaction matrix elements.

II. ELECTRONIC STRUCTURE OF PbSe

In this section we present a four-band envelope-function calculation of the electron and hole states in spherical PbSe

QDs, following the work of Kang and Wise.[25] We also adopt a spherical approximation for the $\mathbf{k}\cdot\mathbf{p}$ Hamiltonian, in order to simplify calculations and to fully exploit the symmetry of the problem. Band anisotropy has been shown to shift the energy of the QD excited states and to provide oscillator strength also to transitions which are forbidden in the isotropic approximation.[26,27] The former effect is not very important for the aim of this work, while the latter can be approximately included in our simulations by broadening the absorption spectrum as discussed in Sec. IV. Lead salts have direct band gaps at four equivalent L points in the Brillouin zone, the bottom of the conduction band, and the top of the valence band having L_6^- and L_6^+ symmetry, respectively, in the double-group notation. Neglecting mixing between states belonging to different L valleys, the Hamiltonian at each L point can be written in the basis of band-edge Bloch functions $\{|L_6^-\uparrow\rangle_\Lambda, |L_6^-\downarrow\rangle_\Lambda, |L_6^+\uparrow\rangle_\Lambda, |L_6^+\downarrow\rangle_\Lambda\}$, where $\Lambda=\{1,2,3,4\}$ denotes the valley. Under the above assumptions the spherical Hamiltonian is given by[25]

$$\hat{H}_0(k) = \begin{bmatrix} \left(\dfrac{E_g^{\text{bulk}}}{2} + \dfrac{\hbar^2 k^2}{2m^-}\right)\boldsymbol{I} & \dfrac{\hbar P}{m}\boldsymbol{k}\cdot\boldsymbol{\sigma} \\ \dfrac{\hbar P}{m}\boldsymbol{k}\cdot\boldsymbol{\sigma} & -\left(\dfrac{E_g^{\text{bulk}}}{2} + \dfrac{\hbar^2 k^2}{2m^+}\right)\boldsymbol{I} \end{bmatrix}, \tag{1}$$

where $\boldsymbol{I}$ is the 2×2 identity matrix, $\boldsymbol{\sigma}$ is the Pauli-spin matrix, E_g^{bulk} is the bulk band gap, m is the free-electron mass, m^- (m^+) is the far-band contribution to the isotropic band-edge effective mass of electrons (holes), and P is an effective (isotropic) value for the momentum-matrix element taken between the extremal valence- and conduction-band states.

Single-particle states are found by solving the eigenvalue equation

$$\hat{H}_0(\mathbf{k})\Psi(\boldsymbol{r}) = E\Psi(\boldsymbol{r}), \tag{2}$$

where the eigenfunctions, $\Psi(\boldsymbol{r})$, can be expressed as the product of a Bloch part and of an envelope part,

$$\Psi(\boldsymbol{r}) = F_1(\boldsymbol{r})|L_6^-\uparrow\rangle_\Lambda + F_2(\boldsymbol{r})|L_6^-\downarrow\rangle_\Lambda + F_3(\boldsymbol{r})|L_6^+\uparrow\rangle_\Lambda + F_4(\boldsymbol{r}) \times |L_6^+\downarrow\rangle_\Lambda. \tag{3}$$

Due to the spherical approximation we can find eigenstates of $\hat{H}_0$ which are at the same time eigenstates of the total angular momentum $\hat{\mathbf{J}}$ and of the parity $\hat{\mathbf{\Pi}}$. Such states will be labeled by their wave vector k, parity π, and total angular-momentum quantum numbers j and m, with the latter being the projection of the total angular momentum j along the z axis. We add that j, being the sum of orbital and spin angular momenta, is half integer and that, for each given value of Λ, the z axis will be oriented along the corresponding $\langle 111\rangle$ direction of the cubic lattice. It is useful, at this point, to introduce the following symmetry adapted basis set for the Bloch and angular part of the wave function:

$$\Omega^C_{\Lambda,\pi,j,m} = \begin{cases} i\sqrt{\dfrac{l+m+1/2}{2l+1}}Y_l^{m-1/2}|L_6^-\uparrow\rangle_\Lambda + i\sqrt{\dfrac{l-m+1/2}{2l+1}}Y_l^{m+1/2}|L_6^-\downarrow\rangle_\Lambda, & l=j-\dfrac{1}{2}\ \text{ if }\ \pi=(-1)^{j+(1/2)} \\ i\sqrt{\dfrac{l-m+1/2}{2l+1}}Y_l^{m-1/2}|L_6^-\uparrow\rangle_\Lambda - i\sqrt{\dfrac{l+m+1/2}{2l+1}}Y_l^{m+1/2}|L_6^-\downarrow\rangle_\Lambda, & l=j+\dfrac{1}{2}\ \text{ if }\ \pi=(-1)^{j-(1/2)} \end{cases}, \tag{4}$$

for the conduction band and

$$\Omega^V_{\Lambda,\pi,j,m} = \begin{cases} \sqrt{\dfrac{l-m+1/2}{2l+1}}Y_l^{m-1/2}|L_6^+\uparrow\rangle_\Lambda - \sqrt{\dfrac{l+m+1/2}{2l+1}}Y_l^{m+1/2}|L_6^+\downarrow\rangle_\Lambda, & l=j+\dfrac{1}{2}\ \text{ if }\ \pi=(-1)^{j+(1/2)} \\ \sqrt{\dfrac{l+m+1/2}{2l+1}}Y_l^{m-1/2}|L_6^+\uparrow\rangle_\Lambda + \sqrt{\dfrac{l-m+1/2}{2l+1}}Y_l^{m+1/2}|L_6^+\downarrow\rangle_\Lambda, & l=j-\dfrac{1}{2}\ \text{ if }\ \pi=(-1)^{j-(1/2)} \end{cases}, \tag{5}$$

for the valence band.

A. Bulk

In the bulk Eq. (2) is solved with the condition that the wave functions vanish as $r\to\infty$. The (non-normalized) bulk eigenfunctions are then given by

$$\psi^C_{\Lambda,k,\pi,j,m}(\boldsymbol{r}) = \begin{cases} j_l(kr)\Omega^C_{\Lambda,\pi,j,m} + C(k)j_{l+1}(kr)\Omega^V_{\Lambda,\pi,j,m}, & l=j-\dfrac{1}{2}\ \text{ if }\ \pi=(-1)^{j+(1/2)} \\ j_l(kr)\Omega^C_{\Lambda,\pi,j,m} + C(k)j_{l-1}(kr)\Omega^V_{\Lambda,\pi,j,m}, & l=j+\dfrac{1}{2}\ \text{ if }\ \pi=(-1)^{j-(1/2)} \end{cases}, \tag{6}$$

$$\psi^{V}_{\Lambda,k,\pi,j,m}(\boldsymbol{r}) = \begin{cases} C(k)j_{l-1}(kr)\Omega^{C}_{\Lambda,\pi,j,m} + j_l(kr)\Omega^{V}_{\Lambda,\pi,j,m}, & l = j + \dfrac{1}{2} \ \text{ if } \ \pi = (-1)^{j+(1/2)} \\[2ex] C(k)j_{l+1}(kr)\Omega^{C}_{\Lambda,\pi,j,m} + j_l(kr)\Omega^{V}_{\Lambda,\pi,j,m}, & l = j - \dfrac{1}{2} \ \text{ if } \ \pi = (-1)^{j-(1/2)} \end{cases}, \tag{7}$$

where j_l are spherical Bessel functions of order l, k is a real wave vector, and

$$C(k) = \frac{2i\tilde{P}k}{E_g^{\text{bulk}} + \dfrac{\hbar^2}{m^-}k^2 - 2E_C(k)} \tag{8}$$

is a coefficient with modulus smaller than unity, where we introduced $\tilde{P} \equiv \hbar P/m$. The corresponding eigenvalues are

$$E^V(k) = \frac{1}{2}\left\{\frac{\hbar^2}{2}\left(\frac{1}{m^-} - \frac{1}{m^+}\right)k^2 - \sqrt{\left[E_g^{\text{bulk}} + \frac{\hbar^2}{2}\left(\frac{1}{m^-} + \frac{1}{m^+}\right)k^2\right]^2 + (2\tilde{P}k)^2}\right\}, \tag{9}$$

$$E^C(k) = \frac{1}{2}\left\{\frac{\hbar^2}{2}\left(\frac{1}{m^-} - \frac{1}{m^+}\right)k^2 + \sqrt{\left[E_g^{\text{bulk}} + \frac{\hbar^2}{2}\left(\frac{1}{m^-} + \frac{1}{m^+}\right)k^2\right]^2 + (2\tilde{P}k)^2}\right\}, \tag{10}$$

for the valence and conduction band, respectively.

B. Quantum dots

In a QD of radius R we solve Eq. (2) with the condition that the wave functions vanish at $r=R$, thus assuming an infinite potential boundary. Such an approximation is useful to simplify calculations and it is also accurate enough for the purposes of the present paper. As a matter of fact, taking into account a finite confining potential does not significantly alter the energy of the single-particle states.[28] In a QD there is no restriction for the behavior as $r \to \infty$ and we obtain new solutions of Eq. (2) from wave functions (6) and (7) by replacing the real wave vector k with a purely imaginary wave vector λ. Such new solutions will contain modified Bessel functions, according to the definition $i_l(x) = i^{-l}j_l(ix)$. In particular we notice that for each real wave vector k it is possible to find two purely imaginary wave vectors $\lambda^C(k)$ and $\lambda^V(k)$ such that $E^C(k) = E^C(\lambda^C(k))$ and $E^V(k) = E^V(\lambda^V(k))$, respectively. As a consequence bulk eigenstates $\psi_{\Lambda,k,\pi,j,m}$ are replaced in a QD by an appropriate superposition $\Psi_{\Lambda,k,\pi,j,m}(\boldsymbol{r}) = \psi_{\Lambda,k,\pi,j,m}(\boldsymbol{r}) + A\,\psi_{\Lambda,\lambda(k),\pi,j,m}(\boldsymbol{r})$. The coefficient A is found by imposing the boundary condition $\Psi_{\Lambda,k,\pi,j,m}(R) = 0$ and solving for k. This procedure yields an infinite number of discrete solutions, hereafter indicated with k_n, so that the continuous quantum number k is replaced by the discrete quantum number n. The (non-normalized) QD eigenfunctions are finally found explicitly as

$$\Psi^{C}_{\Lambda,n,\pi,j,m}(\boldsymbol{r}) = \begin{cases} \left[j_l(k_n r) - \dfrac{j_l(k_n R)}{j_l(\lambda^C_n R)} j_l(\lambda^C_n r)\right]\Omega^{C}_{\Lambda,\pi,j,m} + C(k_n)\left[j_{l+1}(k_n r) - \dfrac{j_{l+1}(k_n R)}{j_{l+1}(\lambda^C_n R)} j_{l+1}(\lambda^C_n r)\right]\Omega^{V}_{\Lambda,\pi,j,m} \\ l = j - \dfrac{1}{2}, \quad \text{if } \ \pi = (-1)^{j+(1/2)}; \\ \left[j_l(k_n r) - \dfrac{j_l(k_n R)}{j_l(\lambda^C_n R)} j_l(\lambda^C_n r)\right]\Omega^{C}_{\Lambda,\pi,j,m} + C(k_n)\left[j_{l-1}(k_n r) - \dfrac{j_{l-1}(k_n R)}{j_{l-1}(\lambda^C_n R)} j_{l-1}(\lambda^C_n r)\right]\Omega^{V}_{\Lambda,\pi,j,m} \\ l = j + \dfrac{1}{2}, \quad \text{if } \ \pi = (-1)^{j-(1/2)}; \end{cases}, \tag{11}$$

$$\Psi^V_{\Lambda,n,\pi,j,m}(\boldsymbol{r})=\begin{cases} C(k_n)\left[j_{l-1}(k_nr)-\dfrac{j_{l-1}(k_nR)}{j_{l-1}(\lambda_n^VR)}j_{l-1}(\lambda_n^Vr)\right]\Omega^C_{\Lambda,\pi,j,m}+\left[j_l(k_nr)-\dfrac{j_l(k_nR)}{j_l(\lambda_n^VR)}j_l(\lambda_n^Vr)\right]\Omega^V_{\Lambda,\pi,j,m} \\ l=j+\dfrac{1}{2}\ \ \text{if}\ \ \pi=(-1)^{j+(1/2)}; \\ C(k_n)\left[j_{l+1}(k_nr)-\dfrac{j_{l+1}(k_nR)}{j_{l+1}(\lambda_n^VR)}j_{l+1}(\lambda_n^Vr)\right]\Omega^C_{\Lambda,\pi,j,m}+\left[j_l(k_nr)-\dfrac{j_l(R)}{j_l(\lambda_n^VR)}j_l(\lambda_n^Vr)\right]\Omega^V_{\Lambda,\pi,j,m} \\ l=j-\dfrac{1}{2}\ \ \text{if}\ \ \pi=(-1)^{j-(1/2)}. \end{cases} \tag{12}$$

In the above equations $\lambda_n^C=\lambda^C(k_n)$, $\lambda_n^V=\lambda^V(k_n)$ and the corresponding energies are given by $E_n^C=E^C(k_n)$ and $E_n^V=E^V(k_n)$ for the conduction and valence-band states, respectively. Each state is $4(2j+1)$ times degenerate since energy does not depend on the quantum numbers Λ and m.

It is customary to label single-particle states in a QD as nl_j even if, as we have explicitly shown, they are only eigenstates of j and contain states with different values of the orbital angular momentum l. In this notation the value of l is assumed to be the one of the most relevant part of the wave function, i.e., the value used in Eqs. (11) and (12). The parity of the wave function for a state nl_j is therefore given by

$$\pi=\begin{cases}(-1)^{l+1}\ \text{for electrons}\\(-1)^{l}\ \text{for holes}\end{cases}.$$

We are aware that the four-band envelope-function formalism is not valid for very small QDs, with radii $R<1.5$ nm, and it is also not very accurate in reproducing the experimental energies of the lowest energy exciton for QD with radii between 1.5 and 3.5 nm.[28] Nevertheless it is a solid theory which allows a full description of the problem in terms of simple wave functions with well defined symmetry properties. This is of fundamental importance in order to understand which states play the most important role in CM, which is the main aim of this work.

III. DIRECT PHOTOGENERATION OF BIEXCITONS AND QUANTUM EFFICIENCY

In this section we present the method adopted to compute the creation rates of QD excited states by solar-type radiation. In our model e-e interaction is treated as a small perturbation to the single-particle Hamiltonian $\hat{H}_0$. The full QD Hamiltonian $\hat{H}$ is therefore

$$\hat{H}=\hat{H}_0+\hat{V}_{ee}, \tag{13}$$

with

$$\hat{V}_{ee}=\sum_{i<j}\frac{e^2}{\epsilon^{\mathrm{QD}}|\hat{\boldsymbol{r}}_i-\hat{\boldsymbol{r}}_j|}, \tag{14}$$

where e is the electron charge, ϵ^{QD} is the QD dielectric constant, $\hat{\boldsymbol{r}}_i$ is the position operator of the ith electron, and the summation in Eq. (14) is taken over all electron pairs. We point out that it is possible to define an average macroscopic dielectric function even for very small QDs, as discussed in the Appendix where a formula to compute ϵ^{QD} is also given. At zero-order approximation, i.e., when e-e interaction is neglected, QD excited states are given by the product of single-particle states (11) and (12) corresponding to electrons and holes, respectively. In the energy range of interest (up to $4E_g$) excited states with one, two and three e-h pairs (triexcitons) should be taken into account. However, due to computational limitations, in the present work we only consider one-exciton and biexciton excited states, denoted in the following as $|x\rangle$ and $|b\rangle$, respectively. We believe that including triexcitons would not alter the main conclusions of this work, as also suggested by recent experiments which found no evidence of triexciton generation at excitation energies as high as $3.7E_g$ in QDs very similar to the ones we consider here.[10] The eigenfunctions of the unperturbed Hamiltonian $\hat{H}_0$ form a complete orthonormal set and they will be used in the following as a basis to describe the eigenfunctions of the full Hamiltonian $\hat{H}$. In particular, in the zero-order approximation, exciton wave functions may be expressed as the direct product of an electron and a hole, while biexcitons are the direct product of two excitons. Since e-e interaction does not depend on time, in the first-order approximation the ground state and biexciton wave functions are

$$\begin{aligned}|0^{(1)}\rangle&=|0^{(0)}\rangle+\sum_{b'}\frac{\langle 0^{(0)}|\hat{V}_{ee}|b'^{(0)}\rangle}{E_0-E_{b'}}|b'^{(0)}\rangle\\&\quad+\sum_{x'}\frac{\langle 0^{(0)}|\hat{V}_{ee}|x'^{(0)}\rangle}{E_0-E_{x'}}|x'^{(0)}\rangle,\end{aligned} \tag{15}$$

and

$$\begin{aligned}|b^{(1)}\rangle&=|b^{(0)}\rangle+\frac{\langle b^{(0)}|\hat{V}_{ee}|0^{(0)}\rangle}{E_b-E_0}|0^{(0)}\rangle+\sum_{x'}\frac{\langle b^{(0)}|\hat{V}_{ee}|x'^{(0)}\rangle}{E_b-E_{x'}}|x'^{(0)}\rangle\\&\quad+\sum_{b'\neq b}\frac{\langle b^{(0)}|\hat{V}_{ee}|b'^{(0)}\rangle}{E_b-E_{b'}}|b'^{(0)}\rangle,\end{aligned} \tag{16}$$

respectively, where the (0) superscript indicates the unperturbed single-particle states. In the above equations and in the following, energies E refer to unperturbed QD states and the superscript (0) is omitted to simplify the notation. We note that when e-e interaction is taken into account the structure of the QD states becomes much more complex, since perturbed excited states are a superposition of unperturbed eigenfunctions with different numbers of electron-hole pairs and with different energies. In particular, we stress that the eigenstates of the full Hamiltonian have not a fixed number of e-h pairs any more. In Ref. 16 e-e interaction is considered as very strong and the authors assumed that high-energy QD excited states "form a coherent superposition with charged excitons of the same energy." In our model, we do not use this hypothesis and e-e interaction can be arbitrary, as long as it remains much smaller than the energy differences between unperturbed excited states.

We now consider the process of absorption of electromagnetic radiation by a QD. Having in mind solar irradiance as the external source, we assume that the electromagnetic radiation has a constant intensity and angular frequency ω. However, we point out that such a continuous-wave approximation is still valid in the case of pulsed optical pumping, provided that the pulse duration is much longer than the dephasing times of the relevant excited states. In the dipole approximation, the electromagnetic interaction $\hat{V}_{em}$ then reads as

$$\hat{V}_{em}(t) = \hat{V}_{em}e^{-i\omega t} + \text{c.c.} = \frac{ie\mathcal{E}}{m\omega}e^{-i\omega t}\mathbf{e}\cdot\hat{\boldsymbol{p}} + \text{c.c.} \tag{17}$$

where $\hat{\boldsymbol{p}}$ is the momentum operator and the electric field is $\bar{\mathcal{E}}=\mathbf{e}\mathcal{E}e^{-i\omega t}+\text{c.c.}$, with $\mathbf{e}$ being the direction of the electric-field polarization. At first order in perturbation theory the absorption rate, W, by a discrete QD excited state $|n\rangle$ of energy E_n is given by the Fermi's golden rule as

$$W(\hbar\omega) = \frac{2\pi}{\hbar}|\langle n|\hat{V}_{em}|0\rangle|^2\delta(E_n - \hbar\omega), \tag{18}$$

where $|0\rangle$ represents the QD ground state. We can also replace the discrete state $|n\rangle$ with a continuum of states $|n(E)\rangle$ with energy E and density $\rho_n(E)$ such that $\int_E\rho_n(E)dE=1$, obtaining

$$W(\hbar\omega) = \frac{2\pi}{\hbar}|\langle n(\hbar\omega)|\hat{V}_{em}|0\rangle|^2\rho_n(\hbar\omega). \tag{19}$$

In the following we will always assume that, when passing from a discrete state to a continuum of states, the wave function does not change even if the energy does; i.e., $|n(E)\rangle \equiv |n\rangle$ and $E_{n(\hbar\omega)}=\hbar\omega$.

When e-e interaction is neglected only single-exciton states can be excited by the radiation since $\langle x^{(0)}|\hat{V}_{em}|0^{(0)}\rangle \neq 0$, while biexcitonic states are forbidden in the dipole approximation; i.e., $\langle b^{(0)}|\hat{V}_{em}|0^{(0)}\rangle=0$. To the leading order in V_{ee}, the rate of exciton creation is therefore

$$W_1(\hbar\omega) = \sum_x \frac{2\pi}{\hbar}|\langle x^{(0)}|\hat{V}_{em}|0\rangle|^2\frac{e^{-(E_x - \hbar\omega)^2/2\sigma_x^2}}{\sigma_x\sqrt{2\pi}}, \tag{20}$$

where $|x^{(0)}\rangle$ are unperturbed QD excitonic states of energy E_x and we assumed a Gaussian density of states $\rho_x(E)=\exp(-(E_x-E)^2/2\sigma_x^2)/(\sigma_x\sqrt{2\pi})$ with full width at half maximum (FWHM) $\Gamma_x\equiv 2\sqrt{2\ln 2}\sigma_x$, in order to account for homogeneous and inhomogeneous broadening as well.

In our calculations we only considered direct intraband and interband transitions, i.e., transitions between electrons and/or holes in the same valley. As a consequence, only direct excitons can be created by the external radiation. This approximation greatly simplifies our numerical calculations, by drastically reducing the number of allowed excitonic and, as we will see, biexcitonic states and it is justified by the fact that indirect transitions are only weakly allowed.[25] Denoting by $\Psi_c\equiv\Psi^C_{\Lambda_c,n_c,\pi_c,j_c,m_c}$ and $\Psi_v\equiv\Psi^V_{\Lambda_v,n_v,\pi_v,j_v,m_v}$ the total wave functions of the single-particle conduction and valence-band states, respectively, selection rules for the creation of the corresponding exciton $|vc\rangle$ are $\Lambda_c=\Lambda_v$, $\Delta j=j_c-j_v=0,\pm 1$, $\Delta m=m_c-m_v=0,\pm 1$, and $\pi_c\pi_v=-1$, which in the usual notation for single-particle states imply $\Delta l=l_c-l_v=0$. The more restrictive selection rule $\Delta j=0$ holds only if the electron and hole effective masses are equal.

As already mentioned, zero-order biexcitonic states $|b^{(0)}\rangle$ are forbidden in the dipole approximation. Nevertheless, when considering first-order ground and biexcitonic states, given by Eqs. (15) and (16), respectively, we obtain, to the first order in V_{ee},

$$\langle b^{(1)}|\hat{V}_{em}|0^{(1)}\rangle = \sum_{x'}\frac{\langle b^{(0)}|\hat{V}_{ee}|x'^{(0)}\rangle\langle x'^{(0)}|\hat{V}_{em}|0^{(0)}\rangle}{E_b - E_{x'}} + \sum_{b'}\frac{\langle b^{(0)}|\hat{V}_{em}|b'^{(0)}\rangle\langle b'^{(0)}|\hat{V}_{ee}|0^{(0)}\rangle}{E_0 - E_{b'}}. \tag{21}$$

In the same approximation, the rate of biexciton creation is therefore

$$W_2(\hbar\omega) = \sum_b \frac{2\pi}{\hbar}\left|\sum_{x'}\frac{\langle b^{(0)}|\hat{V}_{ee}|x'^{(0)}\rangle\langle x'^{(0)}|\hat{V}_{em}|0^{(0)}\rangle}{\hbar\omega - E_{x'} + i\gamma_x} + \right. \left. - \sum_{b'}\frac{\langle b^{(0)}|\hat{V}_{em}|b'^{(0)}\rangle\langle b'^{(0)}|\hat{V}_{ee}|0^{(0)}\rangle}{E_{b'}}\right|^2\frac{e^{-(E_b - \hbar\omega)^2/2\sigma_b^2}}{\sigma_b\sqrt{2\pi}}, \tag{22}$$

where $|b^{(0)}\rangle$ are unperturbed biexcitonic states of energy E_b, $|x'^{(0)}\rangle$ ($|b'^{(0)}\rangle$) are unperturbed virtual excitonic (biexcitonic) states of energy $E_{x'}$ ($E_{b'}$), γ_x is the dissipative width of excitonic states, and we set $E_0\equiv 0$. As already done for excitonic absorption, in deriving Eq. (22) we assumed a Gaussian density of states $\rho_b(E)=\exp(-(E_b-E)^2/2\sigma_b^2)/(\sigma_b\sqrt{2\pi})$ with FWHM $\Gamma_b\equiv 2\sqrt{2\ln 2}\sigma_b$. The replacement of E_b with $\hbar\omega$ in the denominator can be understood by recalling the derivation of Eq. (19) and the comment following it.

We see from Eq. (22) that the creation of a biexciton can take place through two interfering paths, described by the two summations, involving virtual excitons and virtual biexcitons, respectively. The former path corresponds to the absorption of a single photon creating a virtual QD exciton, which in turn is coupled to the final biexcitonic state by e-e interaction. The latter path corresponds to an intraband transition from a virtual biexciton to the final biexciton, made possible by the existence of virtual biexcitons coupled to the ground state by e-e interaction.[24] Please note that in this second path no absorption is involved in the creation of virtual biexcitons, so that the denominator of the corresponding term of Eq. (22), containing the energy difference between ground and virtual states, does not depend on the photon energy and it gives no resonance, in contrast to the virtual exciton term.

Due to parity selection rules, only odd biexcitons are optically allowed. In addition, due to our assumption that only direct excitons are allowed, only biexcitons composed of two direct excitons are allowed, either as final or virtual states. This fact, which can be deduced from the explicit calculations described in the Appendix, greatly reduces the computational complexity of the numerical problem.

The dissipative width of excitonic states γ_x is contributed by all possible processes which destroy them, including processes of scattering, transformation or annihilation. For example, for highly excited one-exciton states the dissipative width includes also Auger processes or inverse Auger processes, as the processes of impact ionization considered as the source of CM in Ref. 1.

Quantum efficiency (QE), η, is defined as the average number of electron-hole pairs created per absorbed photon, in formulas

$$\eta(\hbar\omega) = 1 + \frac{W_2(\hbar\omega)}{W_1(\hbar\omega) + W_2(\hbar\omega)}. \tag{23}$$

Since in the above definition we use the quantity W_2, which describes direct photogeneration of biexcitons, this QE characterizes only instantaneous generation and does not take into account the contribution of impact generation of biexcitons. Nevertheless, in order to allow a direct comparison with experiments, we introduce the excitonic and biexcitonic absorption cross section of a single PbSe QD embedded in a host with refractive index n_h, which can be obtained from the transition rates W_1 and W_2 as

$$\sigma_1(\hbar\omega) = \frac{W_1(\hbar\omega)\hbar\omega}{\bar{S}}, \tag{24}$$

$$\sigma_2(\hbar\omega) = \frac{W_2(\hbar\omega)\hbar\omega}{\bar{S}} \tag{25}$$

where $\bar{S}=cn_h/2\pi\mathcal{E}^2$ is the average energy flux per unit time and per unit surface.

We also define the energy dependent excitonic and biexcitonic density of states, $g_x(\hbar\omega)$ and $g_b(\hbar\omega)$, respectively, taking into account a Gaussian broadening as in Eqs. (20) and (22), obtaining

$$g_x(\hbar\omega) = \sum_x \frac{e^{-(E_x-\hbar\omega)^2/2\sigma_x^2}}{\sigma_x\sqrt{2\pi}}, \tag{26}$$

$$g_b(\hbar\omega) = \sum_b \frac{e^{-(E_b-\hbar\omega)^2/2\sigma_b^2}}{\sigma_b\sqrt{2\pi}}. \tag{27}$$

In our calculations we neglect the influence of QD surface excitations, different trap surface states,[29] and different effects of surface ligands[30] on the excitation dynamics. In more accurate theory, such excitations would have to be considered as virtual states as they can be responsible for the energy transfer from bulk to surface and vice versa. We also do not consider the electron-phonon interaction assuming that its role is reflected in the broadening of exciton and biexciton absorption, which can be deduced from experimental data. Finally, the real shape of QDs may be different from spherical and this effect can be particularly important for small QDs but, again, we assume that deviations from sphericity can be accounted for by adjusting the absorption linewidths Γ_x and Γ_b.

IV. RESULTS AND DISCUSSION

In this section we report and discuss the results of our numerical calculations of CM efficiency in PbSe QDs. We stress again that we will describe the features of only one of the possible CM mechanisms, being understood that different mechanisms have different features. In particular direct biexciton photogeneration predicts an instantaneous CM, which, in the energy range we consider, takes place before any impact ionization process. We simulated three different QD samples which, in the following, will be denoted by KW1, KW2, and EL, respectively. For samples KW1 and KW2, we used a set of parameters taken from Kang and Wise paper,[25] while for sample EL parameters have been taken from Ellingson *et al.*[3] The main difference between the two sets is in the effective masses, which in the case of the EL sample are assumed to be equal for electrons and holes. For KW1 and EL QDs, the radius has been set to $R=1.95$ nm, in order to match the size of the smallest samples studied by Ellingson *et al.*[3] For sample KW2, instead, we assume a larger radius, $R=3$ nm, in order to match the energy gap (E_g) of the above mentioned experimental samples. All the parameters used in the numerical calculations are reported in Table I.

First of all, we computed QD single-particle states with energies up to $4E_g$ according to the procedure described in Sec. II. The energies of the six lowest electron and hole states are reported in Table II. As expected, KW1 and KW2 parameters do not reproduce correctly the experimental gaps, which are 0.91 eV for $R=1.95$ nm and about 0.7 eV for $R=3$ nm.[3] On the other hand, EL parameters have been chosen by the authors of Ref. 3 to match their experimental results for a wide range of QD sizes and they produce a more reasonable agreement with the measured energy gap. We further notice that P and D states are split due to spin-orbit coupling, which is included in our model through the parameter P appearing in $\hat{H}_0$. Having the single-particle states we then built all the unperturbed excitonic and biexcitonic states

TABLE I. Parameters used in the numerical calculations and predicted energy gap (E_g) for the three investigated QDs. The expression used to compute ϵ^{QD} is reported in the Appendix. Other parameters are: $E_g^{\text{bulk}}=0.28$ eV (at 300 K) and $2P_l^2/m=1.7$ eV, for all three samples (Ref. 25).

	KW1	KW2	EL
m/m^-	3.9	3.9	1.5
m/m^+	6.9	6.9	1.5
$2P^2/m$ (eV)	2.6	2.6	3.15
R (nm)	1.95	3	1.95
ϵ^{QD}	11.2	15.7	14.6
E_g (eV)	1.55	0.89	1.03

with energies up to the same cutoff energy of $4E_g$.

Excitonic (σ_1) and biexcitonic (σ_2) absorption cross sections have been finally computed by means of Eqs. (24) and (25), respectively, making use of formulas (20) and (22) and of the procedures described in the Appendix for the calculation of $\hat{V}_{em}$ and $\hat{V}_{ee}$ matrix elements. Again, in evaluating W_1 and W_2, we only included final and intermediate states with energies lower than $4E_g$. Moreover, due to our approximations, we only needed to consider single-valley dipole-allowed excitons and all the single- and two-valley biexcitons. In this way we had a total of 1336 excitons and 295 704 biexcitons for sample KW1, 2152 excitons and 1 061 716 biexcitons for sample KW2, 1528 excitons and 2 308 176 biexcitons for sample EL. Raising the value of the energy cutoff above $4E_g$ would quickly increase the number of states involved, because the density of states is higher at higher energies. This was not possible on our workstation, mainly because handling such a large number of states would require an unreasonably large amount of time.

In numerical calculations we always used $n_h=1$, which is appropriate to QDs in vacuum, but we point out that absorption cross sections for a different host material can be easily deduced from the present results following Eqs. (24) and (25). We also assumed $\gamma_x=\Gamma_x=20$ meV and $\Gamma_b=40$ meV, for samples EL and KW2, while we used $\gamma_x=\Gamma_x=30$ meV and $\Gamma_b=60$ meV for sample KW1, in order to have $\gamma_x=\Gamma_x \approx 0.02E_g$ for all the samples. The above values account for both the homogeneous and inhomogeneous broadenings of the single QD and have been taken two times larger for biexcitons as compared to excitons. Experimental absorption linewidths are usually larger than the above values because they are dominated by size dispersion, which we will take into account separately, as discussed below. As an example, we mention that Koole *et al.*[31] found a FWHM of 55 meV for the first optical transition in highly monodisperse QDs of radius 3.4 nm. We add that will show in the following how the biexcitonic cross section depends on γ_x.

TABLE II. Energies of the lowest lying single-particle conduction-band (CB) and valence-band (VB) states for the three investigated QDs (in eV). For sample EL conduction and valence-band states are degenerate because electron and hole masses are assumed to be equal.

	KW1		KW2		EL
	CB	VB	CB	VB	CB/VB
$1S_{1/2}$	0.617	0.933	0.376	0.516	0.513
$1P_{3/2}$	1.05	1.68	0.578	0.850	0.781
$1P_{1/2}$	1.09	1.70	0.607	0.865	0.838
$1D_{5/2}$	1.58	2.60	0.815	1.25	1.07
$1D_{3/2}$	1.62	2.62	0.850	1.27	1.14
$2S_{1/2}$	1.86	3.05	0.947	1.45	1.24

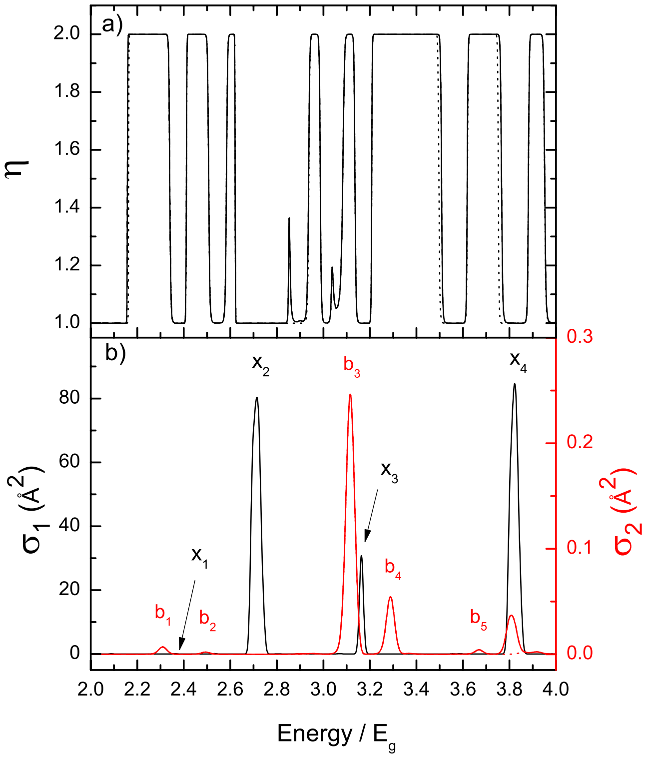

FIG. 1. (Color online) (a) Quantum efficiency, η, as a function of energy computed for KW1 sample using $\gamma_x=\Gamma_x=30$ meV and $\Gamma_b=60$ meV. (b) Excitonic (σ_1) and biexcitonic (σ_2) absorption cross sections as a function of energy computed for KW1 QD using the same parameters as in panel (a). Main excitonic and biexcitonic transitions are labeled for convenience (see text for details). In both panels, (a) and (b), solid lines represent full calculations, dashed lines have been computed by including only the virtual exciton path, and dotted lines have been obtained by including only strongly coupled final biexcitonic states (see text for details).

Figures 1–3 report in solid lines the absorption cross sections and the instantaneous quantum efficiency calculated for the three samples KW1, KW2, and EL, respectively. We first note that for all the samples σ_1 is two to three orders of magnitude larger than σ_2 and that all the relevant biexcitonic absorption peaks correspond to biexcitonic states which are strongly coupled to intense excitonic transitions. Moreover, biexcitonic absorption is enhanced when the final biexcitonic state is resonant with a strongly coupled virtual exciton, as in the case of the peak labeled b_3 in Fig. 1(b) and of the peak at $3.8E_g$ in Fig. 2(b).

In all three QDs quantum efficiencies as large as 2 can be reached in correspondence with allowed biexcitonic transi-

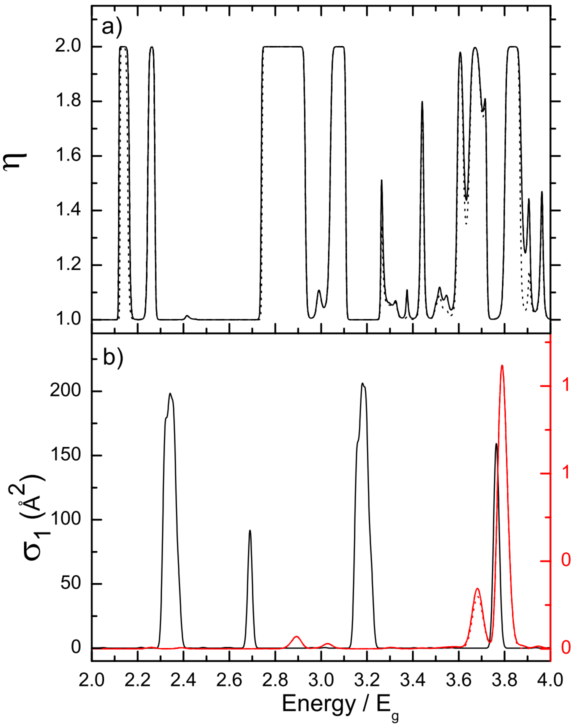

FIG. 2. (Color online) (a) Quantum efficiency, η, as a function of energy computed for KW2 sample using $\gamma_x = \Gamma_x = 20$ meV and $\Gamma_b = 40$ meV. (b) Excitonic (σ_1) and biexcitonic (σ_2) absorption cross sections as a function of energy computed for KW2 QD using the same parameters as in panel (a). In both panels, (a) and (b), solid lines represent full calculations, dashed lines have been computed by including only the virtual exciton path, and dotted lines have been obtained by including only strongly coupled final biexcitonic states (see text for details).

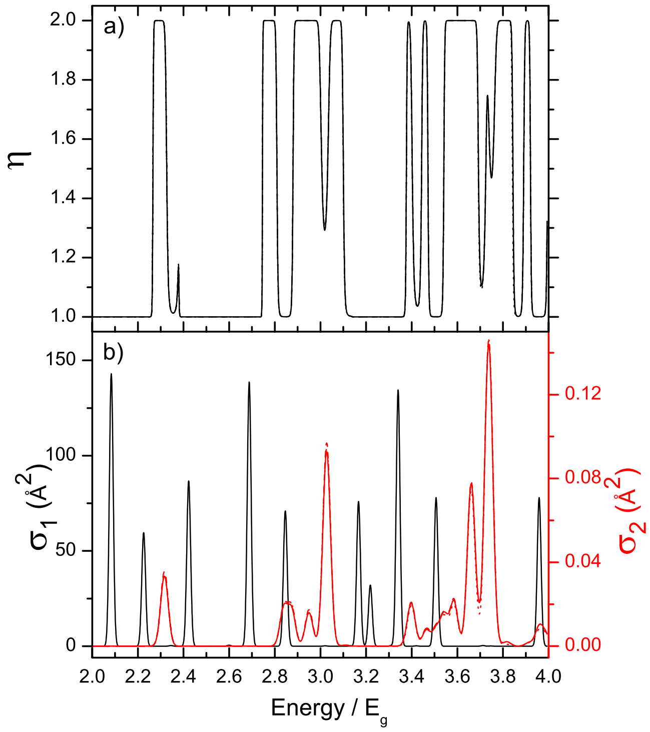

FIG. 3. (Color online) (a) Quantum efficiency, η, as a function of energy computed for EL sample using $\gamma_x = \Gamma_x = 20$ meV and $\Gamma_b = 40$ meV. (b) Excitonic (σ_1) and biexcitonic (σ_2) absorption cross sections as a function of energy computed for EL QD using the same parameters as in panel (a). In both panels, (a) and (b), solid lines represent full calculations, dashed lines have been computed by including only the virtual exciton path, and dotted lines have been obtained by including only strongly coupled final biexcitonic states (see text for details).

tions, but CM is negligible whenever the excitation is resonant with the more intense excitonic transitions. In fact, while it is true that the presence of a resonant virtual excitons enhances biexcitonic absorption, we also found that the number of strongly coupled biexcitonic states is too low to ensure that $\sigma_2 \approx \sigma_1$. We therefore conclude that instantaneous CM can be efficient only when excitonic absorption peaks are largely spaced, as it is the case for small QDs and small excitonic broadenings Γ_x. Unfortunately these conditions are rarely met in real samples in which excitonic absorption is very broad due to size dispersion, nonsphericity, intervalley coupling, thermal motion, and excitonic transitions originating from other points of the Brillouin zone appearing at high energies.[31]

A quantitative comparison between the three samples by means of Figs. 1–3 is not straightforward because the samples have different sizes and broadenings, but we can compare direct biexcitonic photogeneration efficiencies by computing the quantity $\alpha = R^{-3}\int_0^{4E_g}\sigma_2(\hbar\omega)d\hbar\omega$. This quantity is proportional to the total biexcitonic absorption coefficient (up to $4E_g$) in the case of an incident radiation with a uniform spectral density, assuming that the QD volume fraction of the three samples is the same. Note that the spectral range (i.e., 0 to $4E_g$) is different for the three samples but we believe the comparison is still meaningful, because we observe that when energies are scaled to E_g the behavior of samples with the same band structure (KW1 and KW2) is similar. From the computed spectra we found $\alpha = 3.4 \times 10^{-3}$ Å^{-1} meV for sample KW1, 3.7×10^{-3} Å^{-1} meV for KW2, and 2.9×10^{-3} Å^{-1} meV for EL. We are now in a position to discuss the effects of size and band structure. We have already mentioned that the number of states with energies up to $4E_g$ is larger for sample KW2, with $R = 3$ nm, than for sample KW1, with $R = 1.95$ nm. This is a consequence of the single-particle energies scaling with R^{-2} and it is still true when the more correct $R^{-1.5}$ scaling is assumed. We also found that, as expected, Coulomb interaction increases when QD size decreases (see at the end of the Appendix for more details). These two effects have opposite consequences on the biexciton generation and our numerical results show that, for the two sizes we investigated, the net effect is negligible, since we predict very similar values of α for samples KW1 and KW2. Sample EL, on the contrary is the one with the largest number of states and the strongest Coulomb interaction, due to the symmetry between valence and conduction bands (see the Appendix for details). Nevertheless, the total absorption coefficient in this case is predicted to be smaller than in the case of KW samples. In our opinion this is because in the spectral range we investigate the total number of states is still too small to make use of statistical arguments and biexciton generation is due to a limited number of final and intermediate states, whose relative spectral positions strongly affect the final efficiency.

As an aid to the following discussion, hereafter we will explicitly indicate biexcitonic states as $|(e1),(h1),(e2),(h2)\rangle$, where the single-particle notation will be used to describe the two electrons $(e1,e2)$ and the two holes $(h1,h2)$ forming the biexciton. Moreover, if not explicitly stated, by the above notation we will indicate the set of all the degenerate single- and two-valley unperturbed biexcitons that can be built by placing each electron and each hole in whichever valley. In the same spirit we will indicate single-valley (i.e., direct) unperturbed excitons as $|(e),(h)\rangle$. It is now interesting to discuss the threshold for CM. In both samples, KW1 and KW2, the first allowed biexcitonic states are $|1S_{1/2}(e1),1S_{1/2}(h1),1P_{3/2}(e2),1S_{1/2}(h2)\rangle$, with energy 3.53 eV ($2.28E_g$) and 1.99 eV ($2.23E_g$), respectively. As for the EL sample, the first allowed biexcitonic states are $|1S_{1/2}(e1)1S_{1/2}(h1),1S_{1/2}(e2)1P_{1/2}(h2)\rangle$ and $|1S_{1/2}(e1)1S_{1/2}(h1),1P_{1/2}(e2)1S_{1/2}(h2)\rangle$, which are degenerate due to the electron and hole effective masses being equal and have energy 2.38 eV ($2.32E_g$). We can therefore conclude that, even if the three samples have different sizes and effective masses, the threshold for direct biexciton photogeneration, and hence for instantaneous CM, is predicted to be in the same (scaled) energy region, i.e., between 2.2 and $2.4E_g$. Such values are in agreement with the experimental data of Ref. 3 where a statistically significant increase in CM efficiency has been found in the region between 2.1 and $2.9E_g$.

We also investigated the relative contribution of the two interfering virtual paths to biexciton generation. In order to do so, we computed $\sigma_2(\hbar\omega)$ and $\eta(\hbar\omega)$ including only the excitonic virtual path in Eq. (22). Results are shown in Figs. 1–3 with dashed lines. We see that the plots are superimposed to the ones obtained with the full calculations, suggesting that the virtual biexciton path does not contribute significantly to the total transition rate, contrary to what predicted in Ref. 24. This is because some approximations made in Ref. 24 in order to estimate the relative importance of the two paths are not accurate. In particular, it is misleading to assume that only resonant virtual excitonic states contribute to biexciton generation. In fact, our simulations show that the shape of the wave function and the dipole moment of the virtual exciton can be more important than its spectral position in determining how effective its contribution to CM is. As a consequence the number of virtual excitonic states is usually larger than the number of virtual biexcitons, at least in the energy region we investigated. We also found that V_{ee} matrix elements are much smaller in the case of the virtual biexciton path with respect to the virtual exciton path, as discussed in detail in the Appendix.

Another important issue is to determine how many final biexcitonic states are really contributing to the final CM efficiency. We found that in samples KW1, KW2 and EL only 23%, 18%, and 10%, respectively, of all the final biexcitonic states we considered are in fact allowed, as it can be seen in Fig. 4. Moreover, only about one-tenth of the allowed biexcitonic states is indeed significant. In order to demonstrate this point, we considered the virtual exciton path and included in the calculation of σ_2 and η only strongly coupled final biexcitonic states, defined as those states which have a "bulk-screened" V_{ee} matrix element (computed considering $\epsilon^{QD}=\epsilon_{\infty}^{bulk}=23$) of at least 1 meV with some allowed virtual exciton. Strongly coupled biexcitons represent only 3%, 2%, and 1% of all the final biexcitonic states we considered in samples KW1, KW2, and EL, respectively, but we found that they determine almost completely the biexcitonic absorption cross section. The result of the calculations is showed in Figs. 1–3 with dotted lines. The plots are nearly identical to the solid lines obtained by the full calculations, thus confirming that only 1–3 % of all single- and two-valley final biexcitonic states is relevant to direct biexciton photogeneration.

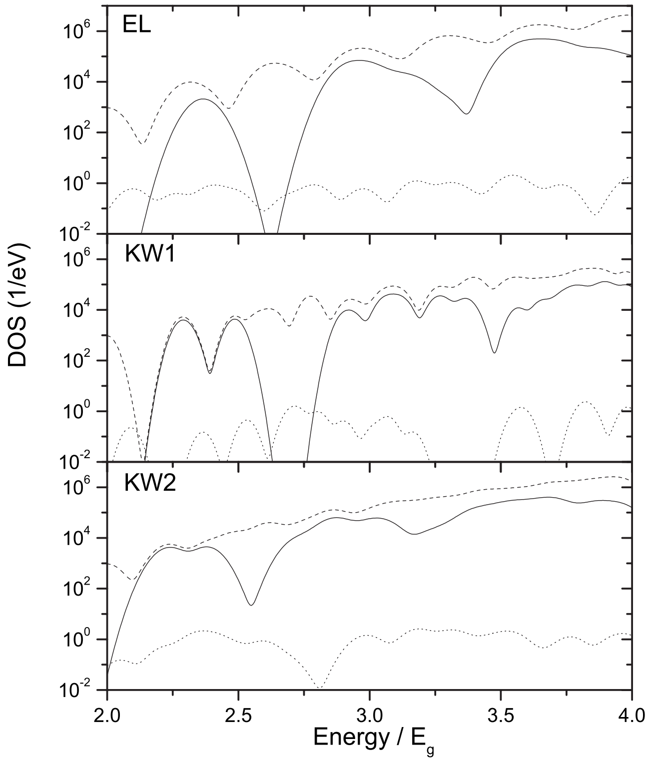

FIG. 4. Density of states of allowed excitons (dotted lines) and allowed single- and two-valley biexcitons (solid lines), computed from Eqs. (26) and (27) with $2\sqrt{2\ln 2}\sigma_x=2\sqrt{2\ln 2}\sigma_b=100$ meV for the three samples. Dashed lines represent the density of all single- and two-valley biexcitons, allowed and not allowed. When all multivalley biexcitons are considered the total density of biexcitonic states is about 16 times the one showed with dashed line.

A more detailed analysis has been performed for sample KW1. In that case biexcitons are largely spaced and it is possible to assign each peak in σ_2 to a well defined set of states. In particular we identified the first five peaks in σ_2, labeled as $b_1,\ldots,b_5$ in Fig. 1, finding that they are all due to final biexcitons composed of three single-particle S states and one P state. Moreover, all of the above biexcitons are allowed mainly through virtual excitons composed exclusively of S holes and electrons. The complete list of biexcitonic states responsible for peaks $b_1,\ldots,b_5$ is reported in Table III, together with the corresponding most relevant virtual excitons. We see from Table III that the most effective virtual excitons are x_0 (i.e., the first allowed excitonic tran-

TABLE III. List of biexcitonic states associated with the first relevant biexcitonic absorption peaks of sample KW1 as labeled in Fig. 1. Virtual excitons are labeled as in Fig. 1 except x_0 which is the first allowed excitons and determines the QD energy gap. Numbers in parenthesis are the exciton energies in units of E_g.

Peak	Energy/E_g	Final biexciton $\|(e1),(h1),(e2),(h2)\rangle$	Virtual excitons $\|(e),(h)\rangle$ (Energy/E_g)
b_1	2.31	$\|1S_{1/2},1S_{1/2},1P_{1/2},1S_{1/2}\rangle$	$x_0:\|1S_{1/2},1S_{1/2}\rangle(1.00)$, $x_1:\|1S_{1/2},2S_{1/2}\rangle(2.36)$
b_2	2.49	$\|1S_{1/2},1S_{1/2},1S_{1/2},1P_{1/2}\rangle$	$x_0:\|1S_{1/2},1S_{1/2}\rangle(1.00)$
b_3	3.12	$\|1P_{1/2},1S_{1/2},2S_{1/2},1S_{1/2}\rangle$	$x_3:\|2S_{1/2},2S_{1/2}\rangle(3.16)$
b_4	3.28	$\|1S_{1/2},1S_{1/2},2S_{1/2},1P_{1/2}\rangle$	$x_3:\|2S_{1/2},2S_{1/2}\rangle(3.16)$
b_5	3.67	$\|1S_{1/2},1S_{1/2},1P_{1/2},2S_{1/2}\rangle$	$x_3:\|2S_{1/2},2S_{1/2}\rangle(3.16)$

sition) and x_3, which are both intense and strongly coupled to the final biexcitonic state. We also notice that these intermediate states are not always resonant with the final states but, when they are, biexcitonic absorption is largely increased, as in the case of the b_3 peak. In order to check the correctness of our analysis we computed $\sigma_2(\hbar\omega)$ including only the final and virtual states reported in the table, finding that they account for about 93% of the total biexciton creation rate up to $3.75E_g$. This confirms that σ_2 and hence the instantaneous CM efficiency are determined by a limited number of strongly coupled biexcitonic states.

The above discussion shows that estimating the rate of biexciton creation based solely on the number of available biexcitonic states can lead to wrong conclusions, at least for excitation energies below $4E_g$. According to our model, for instance, only one- and two-valley biexcitons, representing about 1/16 of all the multivalley biexcitons, can be efficiently generated, being allowed through virtual direct excitons. Moreover, in the region between 2 and $4E_g$, the matrix element of V_{ee} is of the order of 1 meV only for about $1-3$ % of the one- and two-valley biexcitons, while for most of the other states e-e interaction is orders of magnitude smaller. Finally, we have shown that in the case of small QDs, as sample KW1, the list of relevant biexcitonic states is fairly short. All of these findings explain why, in the whole energy region we considered, biexciton creation through the virtual biexciton path is practically negligible and why, in general, biexcitonic transitions are much weaker than excitonic ones.

We now discuss the role of the excitonic dissipative width γ_x. Assuming Γ_x=20 meV and Γ_b=40 meV, for samples EL and KW2, and Γ_x=30 meV and Γ_b=60 meV for sample KW1, we studied what happens as γ_x changes. As expected, the biexciton absorption cross section σ_2 increases as γ_x decreases, but this effect is appreciable only when a biexcitonic final state is in resonance with the virtual excitonic states to which it is more strongly coupled. The results of the calculations are shown in Fig. 5. It can be seen that variations in the cross section can be relevant, but they are limited to narrow spectral regions.

The role of the two parameters Γ_x and Γ_b is to determine the linewidth of the excitonic and biexcitonic absorption peaks, respectively. We already mentioned that in real samples both excitonic and biexcitonic absorption are much broader than we have so far assumed. The main consequence is that, in the whole spectral range, excitonic transitions dominate and the predicted instantaneous CM efficiencies become much smaller than the ones reported in Figs. 1(a), 2(a), and 3(a). More realistic broadenings are considered and discussed below where size dispersion is introduced.

Unfortunately, we are not aware of any study of the resonance structure of CM efficiency, which could provide valuable information on the mechanisms at work. Impact ionization, for instance, can take place only if the excitation is in resonance with a high-energy exciton, in contrast with the direct photogeneration process we have just described. Moreover we are not aware of any experiment where the instantaneous and delayed contributions have been determined separately. However, in order to better compare our simulations with the experimental results, we took into account size

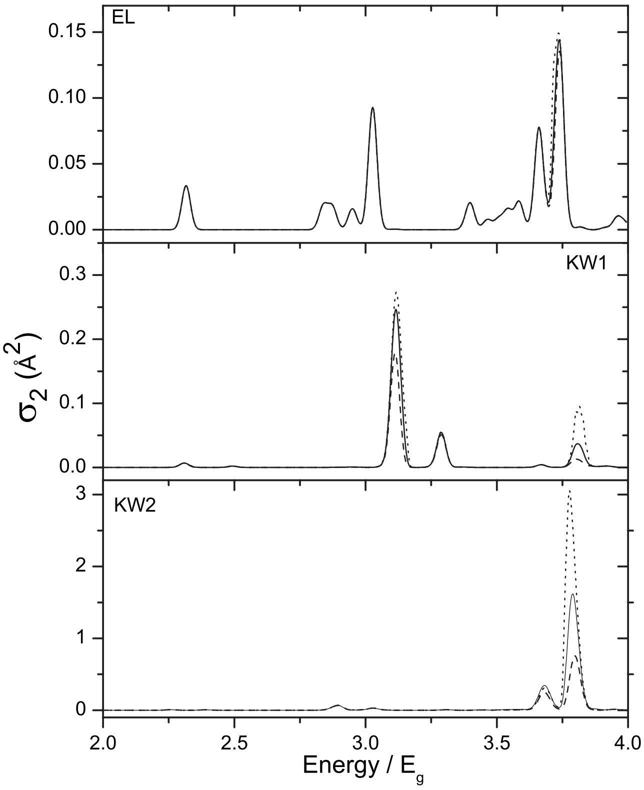

FIG. 5. Biexcitonic absorption cross section, σ_2, as a function of energy computed using Γ_x=20 meV and Γ_b=40 meV (Γ_x=30 meV and Γ_b=60 meV) for samples EL, KW2 (KW1). Plots in dotted, solid and dashed lines have been obtained for samples EL, KW2 (KW1) using dissipative excitonic linewidths γ_x=10 meV (15 meV), γ_x=20 meV (30 meV), and γ_x=40 meV (60 meV), respectively.

dispersion, which is the main source of broadening in real samples. In order to do so without repeating all the numerical calculations for each QD size, we assumed that electromagnetic and Coulomb interactions remain the same for QDs with similar sizes. We took instead into account the change of the energy levels with size. The averaged absorption cross sections are therefore

$$\langle\sigma_1(\hbar\omega)\rangle \equiv \int_r P(r)\sigma_1(r,\hbar\omega)dr, \tag{28}$$

$$\langle\sigma_2(\hbar\omega)\rangle \equiv \int_r P(r)\sigma_2(r,\hbar\omega)dr, \tag{29}$$

where the size distribution $P(r)$ is assumed to be Gaussian with mean QD radius R and relative width σ_R,

$$P(r)dr = \frac{1}{\sigma_R\sqrt{2\pi}}e^{-(r/R-1)^2/2\sigma_R^2}\frac{dr}{R}, \tag{30}$$

and $\sigma_1(r,\hbar\omega)$, $\sigma_2(r,\hbar\omega)$ are obtained from Eqs. (24) and (25) using the following approximate size dependent creation rates:

$$W_1(r,\hbar\omega) = \sum_x \frac{2\pi}{\hbar}|\langle x^{(0)}|\hat{V}_{em}|0\rangle_R|^2\frac{e^{-(E_x(r)-\hbar\omega)^2/2\sigma_x^2}}{\sigma_x\sqrt{2\pi}}, \tag{31}$$

$$W_2(r,\hbar\omega) = \sum_b \frac{2\pi}{\hbar}\left|\sum_{x'}\frac{\langle b^{(0)}|\hat{V}_{ee}|x'^{(0)}\rangle_R\langle x'^{(0)}|\hat{V}_{em}|0^{(0)}\rangle_R}{\hbar\omega - E_{x'}(r) + i\gamma_x} - \sum_{b'}\frac{\langle b^{(0)}|\hat{V}_{em}|b'^{(0)}\rangle_R\langle b'^{(0)}|\hat{V}_{ee}|0^{(0)}\rangle_R}{E_{b'}(r)}\right|^2\frac{e^{-(E_b(r)-\hbar\omega)^2/2\sigma_b^2}}{\sigma_b\sqrt{2\pi}}, \tag{32}$$

where the subscript R indicates that matrix elements have been computed using the mean QD radius.

We show in Figs. 6–8 how absorption cross sections and instantaneous CM efficiencies broaden upon increasing the size dispersion of samples KW1, KW2, and EL, respectively. Such broadening is much larger than both Γ_x and Γ_b so that the averaged line shapes are independent of the values of these parameters. The main consequence is that excitonic absorption is non-negligible in the whole energy range between 2 and $4E_g$ thus significantly reducing the instantaneous CM efficiency, which, for all the samples, drops dramatically as size dispersion increases.

We now compare our predictions to available experimental results. Even when size dispersion is taken into account, excitonic cross sections computed for the two samples with R=1.95 nm (EL and KW1) are of the same order of magnitude as the experimental value of 54 Å^2 measured by Ji *et al.*[33] at 3.1 eV ($3.3E_g$) in QDs of the same size. On the other hand, biexcitonic cross sections are much smaller, leading to the conclusion that in real samples absorption is mainly due to single excitons. This remains true for sample KW2, with R=3 nm, because we know that the absorption cross section scales with the QD volume. From the computed absorption cross sections we can easily estimate the number of directly photogenerated biexcitons. Considering, for instance, a typical pump fluence of about J=1 eV/Å^2 and a biexcitonic absorption cross section σ_2=0.1 Å^2 at $\hbar\omega$=3 eV, we can calculate that about $J\sigma_2/\hbar\omega$=0.03 biexcitons per QD are generated at the sample front surface. Higher fluences would of course lead to the generation of a larger number of biexcitons per QD, but at the same time sequential absorption of more than one exciton by the same QD would become more likely.

A comparison of CM efficiencies is more difficult, because experimental measurements do not separate the contributions of instantaneous and delayed mechanisms. Nair *et*

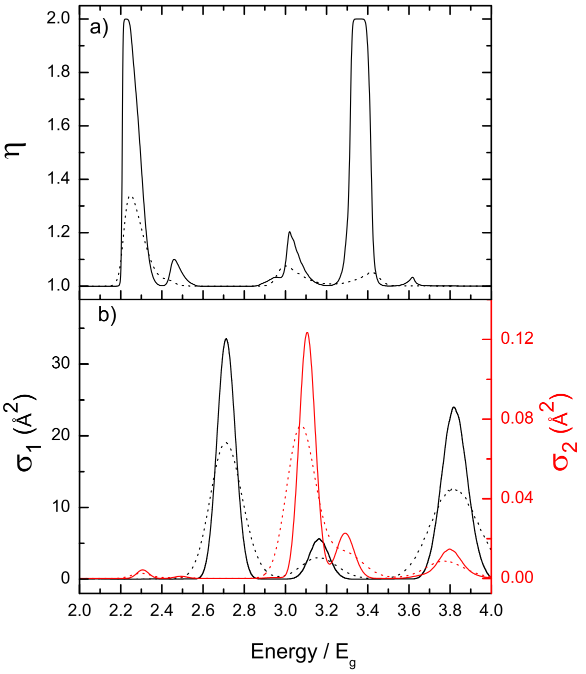

FIG. 6. (Color online) (a) Quantum efficiency, η, as a function of energy computed for KW1 sample using γ_x=Γ_x=30 meV and Γ_b=60 meV. (b) Excitonic (σ_1) and biexcitonic (σ_2) absorption cross sections as a function of energy computed for KW1 QD using the same parameters as in panel (a). In both panels, (a) and (b), plots have been obtained including a size dispersion of 1% (σ_R =0.01, solid lines) and 2% (σ_R=0.02, dotted lines).

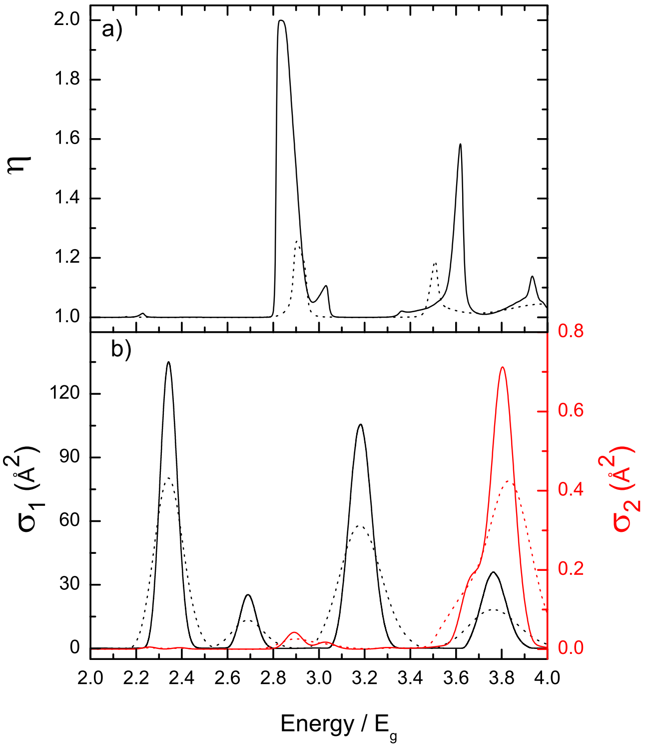

FIG. 7. (Color online) (a) Quantum efficiency, η, as a function of energy computed for KW2 sample using $\gamma_x = \Gamma_x = 20$ meV and $\Gamma_b = 40$ meV. (b) Excitonic (σ_1) and biexcitonic (σ_2) absorption cross sections as a function of energy computed for KW2 QD using the same parameters as in panel (a). In both panels, a) and b), plots have been obtained including a size dispersion of 1% ($\sigma_R = 0.01$, solid lines) and 2% ($\sigma_R = 0.02$, dotted lines).

al.[10] performed transient photoluminescence measurements on PbSe QDs with $E_g = 0.84$ eV, finding $\eta = 1.09$ at $3.69 E_g$. McGuire *et al.*[32] used both time-resolved photoluminescence and transient absorption to determine the QE of PbSe QDs with $E_g = 0.795$ eV, obtaining a value of $\eta = 1.19$ at $3.9 E_g$. Finally, Ji *et al.*[33] measured a QE of 1.6 at $3.26 E_g$ in colloidal PbSe QDs with $E_g = 0.94$ eV by means of spectrally resolved intraband transient absorption. These experimental results, as well as others obtained on similar samples,[1,3] can be compared with the values reported in Figs. 6(a), 7(a), and 8(a), where CM efficiency, i.e., the average number of excitons created per absorbed photon, is plotted as a function of the photon energy. It must be kept in mind, however, that our calculations only give the instantaneous, and not the total, CM efficiency. Generally speaking, we can say that measured efficiencies are comparable with our predictions, at least if size dispersion is not too large. Nevertheless, according to our model, high CM efficiencies correspond to very low total absorption cross sections, much lower than the ones experimentally observed. Thus we conclude that impact ionization is probably the most effective mechanism to obtain CM at long times (>1 ps). We also believe that, at some frequencies, a non-negligible initial population of instantaneously photogenerated biexcitons can improve CM efficiency. In order to investigate the real impact of direct photogeneration energy resolved measurements on highly monodisperse samples would be needed.

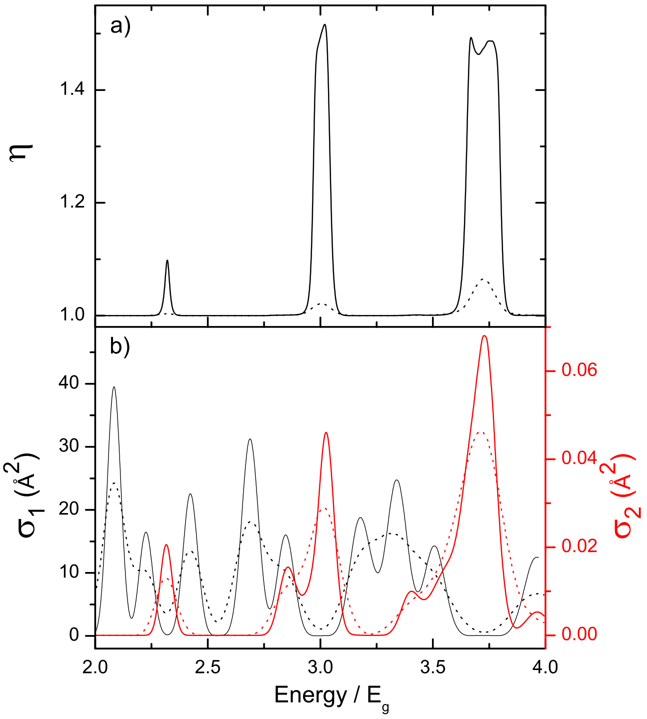

FIG. 8. (Color online) (a) Quantum efficiency, η, as a function of energy computed for EL sample using $\gamma_x = \Gamma_x = 20$ meV and $\Gamma_b = 40$ meV. (b) Excitonic (σ_1) and biexcitonic (σ_2) absorption cross sections as a function of energy computed for EL QD using the same parameters as in panel (a). In both panels, (a) and (b), plots have been obtained including a size dispersion of 1% ($\sigma_R = 0.01$, solid lines) and 2% ($\sigma_R = 0.02$, dotted lines).

V. CONCLUSIONS

The aim of the numerical simulations presented in this paper was to demonstrate the possibility of an instantaneous direct photogeneration of multiple e-h pairs via virtual excitons and biexcitons. It was shown that this process can indeed be efficient for photons in spectral regions of weak QD absorption. In general we reckon that the main mechanism of photogeneration of multiple e-h pairs is, probably, the process of impact ionization[1,14,15] which, however, is not instantaneous. In our simulations of direct photogeneration of multiple e-h pairs via virtual states we did not make use of any *a priori* hypothesis (model) on the structure of the excited state created by the absorbed photon, but our approach presents other limitations which need to be addressed. The parameters we have used in our calculations for spherical nanocrystals[3,25] do not reproduce exactly the experimental e-h spectra of PbSe QDs. Also, in our calculations we took into account e-e interaction only up to the first order of perturbation theory, thus neglecting higher order corrections. Nevertheless, the results of our simulations clearly indicate that in monodisperse PbSe QDs instantaneous CM can be relevant. Numerical calculations allow to estimate the expected value of instantaneous CM efficiency for spherical QDs of different sizes and to understand the dependence of CM efficiency on the parameters determining the optical properties of QDs. The obtained results demonstrate that in the range of incident photon energies we considered (from 2 to $4E_g$) instantaneous CM efficiency strongly depends on frequency and, as expected [see Eq. (23)], it can be particularly large in those spectral regions where dipole-allowed excitonic transitions are weak. Unfortunately, experimental data for CM as well as for the optical properties of QDs are only available for structures in which the QDs are possibly nonspherical (this effect is particularly important for very small QDs) and the interaction of the QDs with the solvent molecules is often substantial. Most importantly, typical experimental samples present a non-negligible size dispersion. For this reason, in order to compare our numerical results with the experiments, we included size dispersion in our treatment by means of a convenient approximation, finding that the predicted one step biexcitonic absorption cross sections are too small to explain the measured CM efficiencies at long times. Nevertheless, we believe that efficient direct biexciton generation can improve CM at long times by creating a non-negligible initial population of biexcitons, at least at some frequencies. In order to clarify the role of the different mechanisms of direct photogeneration of e-h pairs in QDs and to estimate their relative contribution further experimental and theoretical efforts will be needed. Our theory of one step MEG is rather transparent and opens clearly visible avenues for extension and better approximation of the wave functions based on more realistic boundary conditions. It is possible, for instance, to include finite potential barriers, electron-phonon interactions in the high-energy states, nonsphericity, and so on.

ACKNOWLEDGMENT

V.M.A. acknowledges partial support through a Grant from the Russian Foundation of Basic Research.

APPENDIX: EVALUATION OF ELECTROMAGNETIC AND ELECTRON-ELECTRON INTERACTIONS

In this section we give the explicit expressions used to compute the matrix elements of electromagnetic and electron-electron interaction between unperturbed QD states. In the following we will denote conduction (valence) band single-particle states by a single label $c(v)$, indicating the wave function $\Psi_c \equiv \Psi^C_{\Lambda_c,n_c,\pi_c,j_c,m_c}$ ($\Psi_v \equiv \Psi^V_{\Lambda_v,n_v,\pi_v,j_v,m_v}$) and the corresponding collective quantum numbers. In the same spirit, excitonic states will be indicated by the notation $|vc\rangle$ and biexcitonic states by $|v'c';v''c''\rangle$. We will also make use of the fact that each wave function can be written as the product of a Bloch part and of an envelope part, according to definition (3). In particular, it is possible to break spatial integrals into the sum of a short-range and a long-range part, using the property that envelope functions vary slowly over a unit cell. We finally point out that in numerical calculations we used expressions (11) and (12) for unperturbed single-particle QD wave functions taking also into account the proper normalization factors.

Electromagnetic interaction between single-particle states has been computed assuming that only direct dipole transitions are allowed. The relevant matrix elements are[25]

$$\begin{aligned}\langle \Psi_\beta | \hat{V}_{em} | \Psi_\alpha \rangle &= \delta_{\Lambda_\alpha,\Lambda_\beta} \frac{ie\mathcal{E}e^{-i\omega t}}{m\omega} \langle \Psi_\beta(\boldsymbol{r}) | \mathbf{e}\cdot\boldsymbol{p} | \Psi_\alpha(\boldsymbol{r}) \rangle \\ &= \delta_{\Lambda_\alpha,\Lambda_\beta} \frac{ie\mathcal{E}e^{-i\omega t}}{m\omega} \int [F_i^\beta(\boldsymbol{r})]^* (\mathbf{e}\cdot\boldsymbol{p}) F_i^\alpha(\boldsymbol{r}) \\ &\quad + (\mathbf{e}\cdot\hat{z}) P_l \times \{ [F_1^\beta(\boldsymbol{r})]^* F_3^\alpha(\boldsymbol{r}) + [F_3^\beta(\boldsymbol{r})]^* F_1^\alpha(\boldsymbol{r}) \\ &\quad - [F_2^\beta(\boldsymbol{r})]^* F_4^\alpha(\boldsymbol{r}) - [F_4^\beta(\boldsymbol{r})]^* F_2^\alpha(\boldsymbol{r}) \} d\boldsymbol{r}, \qquad \text{(A1)}\end{aligned}$$

where $\alpha=\{c,v\}$ and $\beta=\{c',v'\}$ denote single-particle states which can belong to two different bands or to the same band, giving rise to either interband or intraband transitions, respectively. In the above formula [Eq. (A1)] P_l is the longitudinal Kane momentum-matrix element between the conduction and valence-band-edge Bloch functions and $\hat{z}$ is the $\langle 111 \rangle$ direction of the L valley where the direct transition takes place. Selection rules for photon absorption are: $\Delta j = j_\alpha - j_\beta = 0, \pm 1$, $\Delta m = m_\alpha - m_\beta = 0, \pm 1$, and $\pi_\alpha \pi_\beta = -1$. Focusing on interband transitions we see that the above requirements imply $\Delta l = 0$, while the more restrictive selection rule $\Delta n = 0$ only holds if states with purely imaginary wave vectors λ are neglected and $\Delta j = 0$ only holds if electron and hole effective masses are equal.

Electron-electron interaction between the ground state and a biexciton is explicitly given by

$$\begin{aligned}\langle v'c';v''c'' | \hat{V}_{ee} | 0 \rangle = &= \int\int \Psi^*_{c''}(\boldsymbol{r}_1) \Psi^*_{c'}(\boldsymbol{r}_2) \frac{e^2}{\epsilon^{\mathrm{QD}} |\boldsymbol{r}_1 - \boldsymbol{r}_2|} [\Psi_{v'}(\boldsymbol{r}_1)\Psi_{v''}(\boldsymbol{r}_2) - \Psi_{v''}(\boldsymbol{r}_1)\Psi_{v'}(\boldsymbol{r}_2)] d\mathbf{r}_1 d\mathbf{r}_2 \\ &= \int\int [F_i^{c''}(\boldsymbol{r}_1) F_j^{c'}(\boldsymbol{r}_2)]^* \frac{e^2}{\epsilon^{\mathrm{QD}} |\boldsymbol{r}_1 - \boldsymbol{r}_2|} [F_i^{v'}(\boldsymbol{r}_1) F_j^{v''}(\boldsymbol{r}_2) \delta_{\Lambda_{c''},\Lambda_{v'}} \delta_{\Lambda_{c'},\Lambda_{v''}} - F_i^{v''}(\boldsymbol{r}_1) F_j^{v'}(\boldsymbol{r}_2) \delta_{\Lambda_{c''},\Lambda_{v''}} \delta_{\Lambda_{c'},\Lambda_{v'}}] d\mathbf{r}_1 d\mathbf{r}_2 \\ &\quad + \text{short range terms}, \qquad \text{(A2)}\end{aligned}$$

where summation over repeated indices is assumed and the integrals have been broken into their short- and long-range components. We note that in the above expression Coulomb interaction is given by the sum of two exchange terms and there is no direct interaction. Short range terms are not reported because in all our numerical calculations they have been neglected. It is well known that in PbSe QDs the short-range part of the direct Coulomb interaction is important only for very small clusters with radius $R < 1$ nm.[25] As for exchange terms, it is possible for the long- and short-range components to be of the same order of magnitude, but, since the exchange strength constants of the bulk material, which are needed for a quantitative estimate of the short-range part, are unavailable for PbSe, we preferred to neglect the short-range contribution also for the exchange part of the interaction. Selection rules for the above matrix elements [Eq. (A2)] are $\pi_{v'}\pi_{v''}\pi_{c'}\pi_{c''}=1$ and $m_{v'}+m_{v''}=m_{c'}+m_{c''}$. It is important to point out that, within our approximations, only biexcitons composed of two direct excitons, i.e., excitons with both hole and electron in the same valley, are coupled to the ground state.

Electron-electron interaction between an exciton and a biexciton has been computed as

$$\begin{aligned}
\langle v'c';v''c''|\hat{V}_{ee}|vc\rangle = {} & \delta_{c,c'}\int\int \Psi^*_{c''}(\boldsymbol{r}_1)\Psi^*_{v}(\boldsymbol{r}_2)\frac{e^2}{\epsilon^{\mathrm{QD}}|\boldsymbol{r}_1-\boldsymbol{r}_2|}[\Psi_{v'}(\boldsymbol{r}_1)\Psi_{v''}(\boldsymbol{r}_2)-\Psi_{v''}(\boldsymbol{r}_1)\Psi_{v'}(\boldsymbol{r}_2)]d\mathbf{r}_1d\mathbf{r}_2\\
& +\delta_{c,c''}\int\int \Psi^*_{v}(\boldsymbol{r}_1)\Psi^*_{c'}(\boldsymbol{r}_2)\frac{e^2}{\epsilon^{\mathrm{QD}}|\boldsymbol{r}_1-\boldsymbol{r}_2|}[\Psi_{v'}(\boldsymbol{r}_1)\Psi_{v''}(\boldsymbol{r}_2)-\Psi_{v''}(\boldsymbol{r}_1)\Psi_{v'}(\boldsymbol{r}_2)]d\mathbf{r}_1d\mathbf{r}_2\\
& +\delta_{v,v'}\int\int \Psi^*_{c'}(\boldsymbol{r}_1)\Psi^*_{c''}(\boldsymbol{r}_2)\frac{e^2}{\epsilon^{\mathrm{QD}}|\boldsymbol{r}_1-\boldsymbol{r}_2|}[\Psi_{v''}(\boldsymbol{r}_1)\Psi_{c}(\boldsymbol{r}_2)-\Psi_{c}(\boldsymbol{r}_1)\Psi_{v''}(\boldsymbol{r}_2)]d\mathbf{r}_1d\mathbf{r}_2\\
& +\delta_{v,v''}\int\int \Psi^*_{c'}(\boldsymbol{r}_1)\Psi^*_{c''}(\boldsymbol{r}_2)\frac{e^2}{\epsilon^{\mathrm{QD}}|\boldsymbol{r}_1-\boldsymbol{r}_2|}[\Psi_{c}(\boldsymbol{r}_1)\Psi_{v'}(\boldsymbol{r}_2)-\Psi_{v'}(\boldsymbol{r}_1)\Psi_{c}(\boldsymbol{r}_2)]d\mathbf{r}_1d\mathbf{r}_2\\
= {} & \delta_{c,c'}\int\int [F_i^{c''}(\boldsymbol{r}_1)F_j^{v}(\boldsymbol{r}_2)]^*\frac{e^2}{\epsilon^{\mathrm{QD}}|\boldsymbol{r}_1-\boldsymbol{r}_2|}[F_i^{v'}(\boldsymbol{r}_1)F_j^{v''}(\boldsymbol{r}_2)\delta_{\Lambda_{c''},\Lambda_{v'}}\delta_{\Lambda_{v},\Lambda_{v''}}-F_i^{v''}(\boldsymbol{r}_1)F_j^{v'}(\boldsymbol{r}_2)\delta_{\Lambda_{c''},\Lambda_{v''}}\delta_{\Lambda_{v},\Lambda_{v'}}]d\mathbf{r}_1d\mathbf{r}_2\\
& +\delta_{c,c''}\int\int [F_i^{v}(\boldsymbol{r}_1)F_j^{c'}(\boldsymbol{r}_2)]^*\frac{e^2}{\epsilon^{\mathrm{QD}}|\boldsymbol{r}_1-\boldsymbol{r}_2|}[F_i^{v'}(\boldsymbol{r}_1)F_j^{v''}(\boldsymbol{r}_2)\delta_{\Lambda_{v},\Lambda_{v'}}\delta_{\Lambda_{c'},\Lambda_{v''}}\\
& -F_i^{v''}(\boldsymbol{r}_1)F_j^{v'}(\boldsymbol{r}_2)\delta_{\Lambda_{v},\Lambda_{v''}}\delta_{\Lambda_{c'},\Lambda_{v'}}]d\mathbf{r}_1d\mathbf{r}_2\\
& +\delta_{v,v'}\int\int [F_i^{c'}(\boldsymbol{r}_1)F_j^{c''}(\boldsymbol{r}_2)]^*\frac{e^2}{\epsilon^{\mathrm{QD}}|\boldsymbol{r}_1-\boldsymbol{r}_2|}[F_i^{v''}(\boldsymbol{r}_1)F_j^{c}(\boldsymbol{r}_2)\delta_{\Lambda_{c'},\Lambda_{v''}}\delta_{\Lambda_{c''},\Lambda_{c}}-F_i^{c}(\boldsymbol{r}_1)F_j^{v''}(\boldsymbol{r}_2)\delta_{\Lambda_{c'},\Lambda_{c}}\delta_{\Lambda_{c''},\Lambda_{v''}}]d\mathbf{r}_1d\mathbf{r}_2\\
& +\delta_{v,v''}\int\int [F_i^{c'}(\boldsymbol{r}_1)F_j^{c''}(\boldsymbol{r}_2)]^*\frac{e^2}{\epsilon^{\mathrm{QD}}|\boldsymbol{r}_1-\boldsymbol{r}_2|}[F_i^{c}(\boldsymbol{r}_1)F_j^{v'}(\boldsymbol{r}_2)\delta_{\Lambda_{c'},\Lambda_{c}}\delta_{\Lambda_{c''},\Lambda_{v'}}-F_i^{v'}(\boldsymbol{r}_1)F_j^{c}(\boldsymbol{r}_2)\delta_{\Lambda_{c'},\Lambda_{v'}}\delta_{\Lambda_{c''},\Lambda_{c}}]d\mathbf{r}_1d\mathbf{r}_2\\
& +\text{short range terms},
\end{aligned} \tag{A3}$$

where, again, summation over repeated indices is assumed. The integrals have been broken into their short- and long-range components and also for the above e-e matrix elements [Eq. (A3)] we neglected short-range terms in the numerical calculations. We note that in the above expression each term is not purely direct or exchange, but has a mixed character. For this reason matrix elements [Eq. (A3)] are in general larger than matrix elements [Eq. (A2)]. Selection rules dictate that exciton and biexciton are coupled by e-e interaction only if they have a single-particle state in common. Moreover, within our approximations, direct excitons can only couple to biexcitons composed of two direct excitons. A further selection rule is $\pi_v\pi_c\pi_{v'}\pi_{v''}\pi_{c'}\pi_{c''}=1$ so that odd biexcitons ($\pi_{v'}\pi_{v''}\pi_{c'}\pi_{c''}=-1$) are coupled to odd excitons ($\pi_v\pi_c=-1$).

When wave functions belonging to different valleys appear in the same integral, expressions (11) and (12) need to be transformed in order to represent all the wave functions in the same reference system. In particular, we used the following formulas to transform spherical harmonics Y_{lm} under a rotation $\mathcal{R}$ parameterized by Euler angles α,β,γ (Ref. 34):

$$\mathcal{R}Y_{lm}=\sum_{m'=-l}^{l}D^l_{m'm}(\mathcal{R})Y_{lm'}, \tag{A4}$$

where

$$D^l_{m'm}(\alpha,\beta,\gamma)=e^{-im'\alpha}d^l_{m'm}(\beta)e^{-im\gamma} \tag{A5}$$

and

$$d^l_{m'm}(\beta)=\sqrt{(l+m)!(l-m)!(l+m')!(l-m')!}\sum_k\frac{(-1)^k[\sin(\beta/2)]^{m-m'+2k}[\cos(\beta/2)]^{2l-m+m'-2k}}{k!(l+m'-k)!(l-m-k)!(m-m'+k)!}. \tag{A6}$$

The dielectric constant ϵ^{QD} plays a very important role as it screens long-range e-e interactions. In bulk PbSe the dielectric constant at optical frequencies is $\epsilon_\infty^{\mathrm{bulk}}=23$,[25] but several calculations[35,36] have shown that the average dielectric constant of semiconductor QDs decreases significantly as the size of the dot is reduced, thus enhancing electron-electron interaction. General arguments based on von Laue's theorem[37] and numerical tight binding[37] and pseudopotential[35,38] calculations confirm that a macroscopic average dielectric function can be defined for sizes larger than a few Fermi wavelengths. Moreover both pseudopotential and tight-binding calculations give very similar results for the value of ϵ^{QD} as a function of the QD size in the case of Si nanocrystals.[37] We therefore adopted the following expression for the macroscopic high-frequency dielectric constant:[38]

$$\epsilon^{\mathrm{QD}} \equiv \epsilon_{\infty}^{\mathrm{QD}}(R) = 1 + (\epsilon_{\infty}^{\mathrm{bulk}} - 1)\frac{[E_g^{\mathrm{bulk}} + \Delta E]^2}{[E_g^{\mathrm{QD}}(R) + \Delta E]^2}, \tag{A7}$$

where $E_g^{\mathrm{bulk}} + \Delta E$ is the energy of the first pronounced peak in the bulk absorption spectrum, corresponding to the E_2 transition in PbSe found at 2.73 eV.[39] The values of ϵ^{QD} used in the calculations are showed in Table I for each sample.

We finally report the highest values found for the moduli of $\hat{V}_{ee}$ matrix elements among those used in our numerical calculations. For sample KW2 we found the maxima of $|\langle v'c';v''c''|\hat{V}_{ee}|0\rangle|$ and of $|\langle v'c';v''c''|\hat{V}_{ee}|vc\rangle|$ to be 1.1 and 7.9 meV, respectively. These values increase to 1.5 and 12.6 meV for sample KW1, which has a smaller size. In sample EL mirror symmetry between conduction and valence bands is expected to enhance all the relevant $\hat{V}_{ee}$ matrix elements, which always involve exchange integrals. Indeed, for this sample the two above mentioned maxima are 3.7 and 17.7 meV, respectively.

[1] R. D. Schaller and V. I. Klimov, Phys. Rev. Lett. **92**, 186601 (2004).

[2] R. D. Schaller, V. M. Agranovich, and V. I. Klimov, Nat. Phys. **1**, 189 (2005).

[3] R. Ellingson, M. C. Beard, J. C. Johnson, P. Yu, O. I. Micic, A. J. Nozik, A. Shabaev, and A. L. Efros, Nano Lett. **5**, 865 (2005).

[4] M. Wolf, R. Brendel, J. H. Werner, and H. J. Queisser, J. Appl. Phys. **83**, 4213 (1998).

[5] R. D. Schaller, M. Petruska, and V. I. Klimov, Appl. Phys. Lett. **87**, 253102 (2005).

[6] R. D. Schaller, M. Sikora, S. Jeong, and V. I. Klimov, J. Phys. Chem. B **110**, 25332 (2006).

[7] J. J. H. Pijpers *et al.*, J. Phys. Chem. C **111**, 4146 (2007).

[8] R. D. Schaller, J. M. Pietryga, and V. I. Klimov, Nano Lett. **7**, 3469 (2007).

[9] M. C. Beard, K. P. Knutsen, P. Yu, J. M. Luther, Q. Song, W. K. Metzger, R. J. Ellingson, and A. J. Nozik, Nano Lett. **7**, 2506 (2007).

[10] G. Nair, S. M. Geyer, L.-Y. Chang, and M. G. Bawendi, Phys. Rev. B **78**, 125325 (2008).

[11] G. Nair and M. G. Bawendi, Phys. Rev. B **76**, 081304(R) (2007).

[12] J. J. H. Pijpers, R. Ulbricht, K. J. Tielrooij, A. Osherov, Y. Golan, C. Delerue, G. Allan, and M. Bonn, Nat. Phys. **5**, 811 (2009).

[13] G. Allan and C. Delerue, Phys. Rev. B **77**, 125340 (2008).

[14] A. Franceschetti, J. M. An, and A. Zunger, Nano Lett. **6**, 2191 (2006).

[15] G. Allan and C. Delerue, Phys. Rev. B **73**, 205423 (2006).

[16] A. Shabaev, A. L. Efros, and A. J. Nozik, Nano Lett. **6**, 2856 (2006).

[17] A. J. Nozik, *Nanostructured and Photoelectrochemical Systems for Solar Photon Conversion* (Imperial College Press, London, 2008), Chap. 3.

[18] E. Fermi, Prog. Theor. Phys. **5**, 570 (1950).

[19] S. V. Kilina, D. S. Kilin, and O. V. Prezhdo, ACS Nano **3**, 93 (2009).

[20] B. L. Wehrenberg, C. Wang, and P. Guyot-Sionnest, J. Phys. Chem. B **106**, 10634 (2002).

[21] R. D. Schaller, J. M. Pietryga, S. V. Goupalov, M. A. Petruska, S. A. Ivanov, and V. I. Klimov, Phys. Rev. Lett. **95**, 196401 (2005).

[22] T. Okuno, Y. Masumoto, M. Ikezawa, T. Ogawa, and A. A. Lipovskii, Appl. Phys. Lett. **77**, 504 (2000).

[23] J. M. Harbold, H. Du, T. D. Krauss, K.-S. Cho, C. B. Murray, and F. W. Wise, Phys. Rev. B **72**, 195312 (2005).

[24] V. I. Rupasov and V. I. Klimov, Phys. Rev. B **76**, 125321 (2007).

[25] I. Kang and F. W. Wise, J. Opt. Soc. Am. B **14**, 1632 (1997).

[26] A. D. Andreev and A. A. Lipovskii, Phys. Rev. B **59**, 15402 (1999).

[27] G. E. Tudury, M. V. Marquezini, L. G. Ferreira, L. C. Barbosa, and C. L. Cesar, Phys. Rev. B **62**, 7357 (2000).

[28] A. Lipovskii *et al.*, Appl. Phys. Lett. **71**, 3406 (1997).

[29] S. Li, M. L. Steigerwald, and L. E. Brus, ACS Nano **3**, 1267 (2009).

[30] S. Killina, S. Ivanov, and S. Tretiak, J. Am. Chem. Soc. (to be published).

[31] R. Koole, G. Allan, C. Delerue, A. Meijerink, D. Vanmaekelbergh, and A. J. Houtepen, Small **4**, 127 (2007).

[32] J. McGuire, J. Joo, J. Pietryga, R. Shaller, and V. Klimov, Acc. Chem. Res. **41**, 1810 (2008).

[33] M. Ji, S. Park, S. T. Connor, T. Mokari, Y. Cui, and K. J. Gaffney, Nano Lett. **9**, 1217 (2009).

[34] G. F. Torres del Castillo, *3-D Spinors, Spin-weighted Functions and Their Applications*, Progress in Mathematical Physics (Birkhäuser, Boston, MA, 2003), Vol. 32.

[35] L.-W. Wang and A. Zunger, Phys. Rev. Lett. **73**, 1039 (1994).

[36] M. Lannoo, C. Delerue, and G. Allan, Phys. Rev. Lett. **74**, 3415 (1995).

[37] C. Delerue, M. Lannoo, and G. Allan, Phys. Rev. B **68**, 115411 (2003).

[38] A. Franceschetti, H. Fu, L.-W. Wang, and A. Zunger, Phys. Rev. B **60**, 1819 (1999).

[39] N. Suzuki, K. Sawai, and S. Adachi, J. Appl. Phys. **77**, 1249 (1995).